Scientific Research Publishing

Open Journal of Fluid Dynamics, 2026, 16(1), 1-19
https://www.scirp.org/journal/ojfd
ISSN Online: 2165-3860
ISSN Print: 2165-3852

# Forced-Air Jet Misalignment at a Photovoltaic Chimney Outlet: Impacts on Heat Transfer and Indoor Airflow

**Kodjo Kpode[1*], Momath Ndiaye[2], Yawovi Nougblega[3], Djoirka Minto Dimoune[4], Aguichi Yombou[1]**

[1]Materials, Renewable Energies and Environment Laboratory, University of Kara, Kara, Togo
[2]Department of Hydraulics, University of Sine Saloum El Hadj Ibrahima Niass, Kaolack, Senegal
[3]Solar Energy Laboratory/Phenomena of Transfer and Energetics Group, University of Lomé, Lomé, Togo
[4]Nansen Tutu Center for Marine Environmental Research, Department of Oceanography, University of Cape Town, Rondebosch, Cape Town, South Africa
Email: *kodjokpode@univkara.tg

**How to cite this paper:** Kpode, K., Ndiaye, M., Nougblega, Y., Dimoune, D.M. and Yombou, A. (2026) Forced-Air Jet Misalignment at a Photovoltaic Chimney Outlet: Impacts on Heat Transfer and Indoor Airflow. *Open Journal of Fluid Dynamics*, **16**, 1-19.
https://doi.org/10.4236/ojfd.2026.161001

**Received:** December 2, 2025
**Accepted:** January 11, 2026
**Published:** January 14, 2026



## Abstract

In solar chimneys, heat released by the absorber plate warms the air, enabling natural ventilation driven by thermal buoyancy. However, such systems are often prone to reverse flow phenomena, which reduce the effectiveness of air renewal. To address this limitation, a photovoltaic (PV) chimney is proposed. This active yet autonomous ventilation system features walls comprising a glass surface and a PV panel connected to an extractor fan at the chimney outlet. The PV panel replaces the conventional absorber by simultaneously providing heat to warm the air and generating electricity to drive forced extraction. The present study quantifies the impact of forced air jet misalignment at the chimney outlet on system performance, with particular attention to the onset of reverse flow and recirculation patterns. Here, misalignment is defined as the deviation of the jet orientation from the chimney axis. The physical phenomena are modeled using the governing equations for laminar forced convection, solved numerically via the finite volume method. Simulations are performed with a Fortran-based computational code for a fixed Reynolds number of $Re = 50$, while varying the jet orientation angle from 0˚ to 66˚ relative to the chimney axis. The results indicate that increasing jet misalignment promotes the formation of secondary flow structures, notably recirculation zones and reverse flow within the system. Consequently, both the heat transfer rate between the PV panel and the air and the airflow rate decrease as the forced jet deviates from the chimney axis.

**Keywords**

Jet Misalignment, Solar Chimney, Photovoltaic Chimney, Active Chimney, Mixed Convection, Recirculation Flows, Reverse Flows

## 1. Introduction

Among the various technologies developed to enhance both energy efficiency and indoor comfort in buildings, the solar chimney represents a promising passive solution. Particularly suitable for dwellings in regions with high solar exposure, this system operates based on the thermosiphon principle. It significantly influences heat transfer and indoor air movement, and has been shown to reduce cooling energy demand by more than 14% [1] [2].

Over the past decade, research has increasingly focused on optimizing this system by strengthening the thermal buoyancy forces responsible for natural ventilation. In most configurations, the chimney walls consist of a glazed surface on one side and a thermal absorber and/or photovoltaic (PV) panel on the opposite side [3]-[9]. When exposed to sunlight through the glass, the absorber heats up and transfers additional thermal energy to the circulating air. In reference [8], the absorber plate is perforated, allowing the mass flow rate to increase by approximately 35% compared to a conventional chimney. This enhanced airflow improves heat removal and overall performance.

Several studies have demonstrated correlations between the outlet airflow rate, heat flux density, and the Rayleigh number [9]-[12]. As solar radiation increases, so does the outlet velocity. The Nusselt number, describing heat exchange between the channel walls and the air, also increases with heat flux [13] [14]. For instance, Ren *et al.* [13] improved ventilation performance by integrating discrete heat sources into the chimney walls, which prevented reverse flows.

Parametric geometric analyses show that the inclination angle, chimney dimensions, and air gap are strongly interdependent [3] [14]. Jing *et al.* [14] identified an optimal air-gap-to-height ratio of 0.5 for a vertical chimney, while Abdeen *et al.* [3] reported an optimal ratio of approximately 0.15 for a 75˚ inclination. Imran *et al.* [12] observed that at 750 W/m$^2$ of solar radiation and a 50 mm air gap, a 60˚ inclination yields a maximum air velocity of about 0.8 m/s. When the air gap was increased to 150 mm, no reverse flow was detected. The inclination angle is particularly important [15], as it affects both the vertical component of buoyancy forces and the amount of solar energy received by the absorber. In general, the angle of maximum irradiation corresponds to the local latitude. In West African regions near the equator, this optimal angle ranges between 0˚ and 15˚ [16]. Deviations of ±20˚ from the latitude result in irradiance losses below 5%. For instance, in a region of Ghana located at 17˚ latitude, the annual optimal angle is around 26.8˚, with only a 1% irradiance loss compared to the monthly optimum [17]. For Cameroon (latitudes 4˚ to 5˚), Ekoe A Akata *et al.* [18] recommend a PV tilt between

10˚ and 20˚ with a south orientation. However, the inclination angle optimizing airflow does not necessarily coincide with the optimum angle for solar radiation, especially because airflow is also affected by seasonal and meteorological variations. Studies conducted at mid to high latitudes (typically above 20˚) often report optimal chimney inclinations between 40˚ and 60˚. For example, Abdallah *et al.* [19] observed that optimal airflow at 27.3˚N occurred at 40˚, while performance declined at 70˚. Bassiouny and Nader [20], working at 28.4˚ latitude, reported optimal airflow between 45˚ and 70˚. Harris and Helwig [21] found that airflow was maximized at angles above 67.5˚, although maximum solar radiation occurred at 22˚ (the site latitude). Similarly, Kong *et al.* [22] showed that the optimal inclination for three Australian cities varied between 45˚ and 60˚ depending on latitude and season. In tropical climates, Ardila *et al.* [23] reported that an inclination of 55˚ provided optimal thermal comfort during several months of the year in Bucaramanga, Colombia, although performance decreased during the most critical month (September). These differences between optimal angles for solar radiation and for airflow are therefore not contradictory, as they result from the combined effects of latitude, seasonal variations, and the competing influences of solar gain and buoyancy-driven flow dynamics.

Another key limitation identified in the literature is the occurrence of reverse and recirculation flows, which prevent continuous air renewal and can lead to thermal discomfort. Such secondary flows tend to arise when the channel width or outlet openings are excessively large. Using an improved predictive method, Hou *et al.* [24] identified an optimal gap-to-height ratio of 0.4 over a tested range of 0.1 to 0.5. Jing *et al.* [14], using another method, had previously found an optimal ratio of 0.5 for gaps between 0.2 and 0.6. Beyond these ratios, reverse flows develop and penetrate deeper into the chimney as the gap increases. Chimney height also influences ventilation, and although no critical height is clearly defined, the width-to-height ratio plays a key role. Generally, taller chimneys increase airflow, but Jing *et al.* [14] recommend maintaining a ratio of 0.5 to avoid reverse flow at the outlet. Conversely, Nguyen and Wells [25] showed that at low width-to-height ratios and constant Rayleigh number, flow separation zones can occur. Inclination relative to the vertical is another trigger for reverse or recirculating flows. Outlet velocity tends to increase with inclination angles closer to 90˚ [22] [26], but this trend is not always observed. When the chimney is inclined, the vertical component of buoyancy decreases, which may promote reverse flows and separation zones [27]. These results are not contradictory: the occurrence of secondary flows depends on both the Rayleigh number and inclination angle. Ren *et al.* [13] observed that increasing the angle between the absorber and the horizontal from 45˚ to 90˚ at constant Rayleigh number led to the progressive emergence of reverse flows. Under low heat flux or reduced Rayleigh number, buoyancy forces may be insufficient to overcome gravity, viscosity, and inertia, making reverse flow more likely. Nguyen [28] reported reverse flows at a Rayleigh number of about $10^6$ for a height-to-gap ratio of 5, while Ren *et al.* [13] observed the same

phenomenon at $Ra = 5 \times 10^6$ and an inclination of 75˚. The intensity of reverse flows increases when both the Rayleigh number and inclination angle rise simultaneously. Reverse flow may thus occur at any Rayleigh number, even at high values where buoyancy would normally dominate. For instance, within *Ra* values from $10^9$ to $10^{11}$, Rakesh and Chengwang [29] detected reverse flows at the chimney outlet, with penetration depth increasing with Rayleigh number. These findings highlight that geometrical and thermal parameters are highly interdependent, making the control of reverse flows challenging in passive systems.

However, Kpode *et al.* [30] demonstrated that controlling the outlet jet velocity can effectively suppress reverse flows and reduce recirculation. Their analysis implicitly assumes alignment of the outlet jet with the chimney axis, thereby limiting the general applicability of their conclusions. In practical systems, however, the jet orientation may deviate from the chimney axis due to design constraints, fan placement, installation tolerances, or deliberate flow-control strategies. Such misalignment can alter flow stability and heat transfer characteristics, potentially promoting the development of reverse flows and recirculation regions, thereby degrading chimney performance. A systematic investigation of the exhaust angle is therefore required to assess how flow stability, heat transfer, and ventilation performance are affected by jet misalignment, and to identify configurations that remain effective under non-ideal operating conditions.

## 2. Methodology

### 2.1. Physical Domain

The physical domain depicted in **Figure 1** is similar to that studied by Kpode *et al.* [30]. It is composed of a rectangular enclosure and an adjacent chimney inclined at 9˚ to the horizontal. This inclination angle corresponds to the recommended value [16] to maximize the irradiation of photovoltaic (PV) panels in a West African country located between latitudes 0˚ and 15˚, characterized by high solar insolation. The chimney is an air duct with a thickness e, formed by a glazed wall and a photovoltaic panel. Through the glazed wall, the PV panel receives solar radiation $\Phi_i$, part of which is converted into heat transferred to the air circulating within the chimney, while the other part is converted into electricity. The generated electricity powers a fan that imposes an outgoing air jet with a velocity $\boldsymbol{V}_{out}$, oriented at an angle $\sigma$ relative to the chimney axis.

### 2.2. Assumptions and Equations

The habitat model is represented as a cavity with walls exposed to a constant heat flux, except for the right lateral wall and the horizontal wall, which are respectively insulated and cooled. The flow is assumed to be laminar, and the Boussinesq approximation is applied. Under these conditions, corresponding to low buoyancy and low flow velocity with a Reynolds number of $Re \approx 45$, optimal ventilation performance can be achieved for this configuration [30]. The amplitude of the outlet velocity, denoted $V_{out}$, is imposed by the fan. From this value, a reference

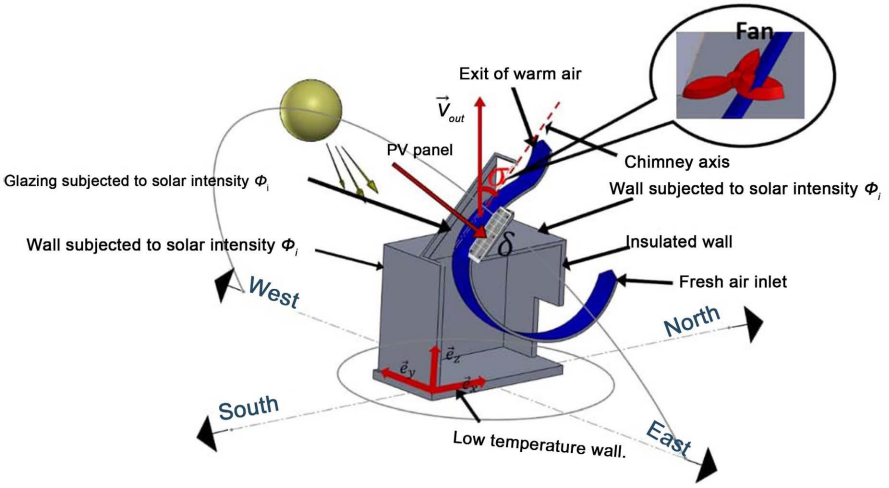


**Figure 1.** Physical domain: adapted from prior studies [30].

time $L/V_{out}$, and a reference temperature gradient $\Phi_i L/\lambda$ are defined, where $L$ and $\lambda$ represent the cavity length and the thermal conductivity of air, respectively. Using these reference parameters, the dimensionless governing equations, namely the continuity, momentum, and energy equations, can be written as follows:

$$\nabla \cdot \nabla \psi = -\Omega \tag{1}$$

$$\frac{\partial \Omega}{\partial t} + \nabla\left(\boldsymbol{V}\cdot\Omega - \frac{1}{Re}\nabla\Omega\right) = -\frac{Ra}{Pe\cdot Re}\frac{\partial \theta}{\partial x} \tag{2}$$

$$\frac{\partial \theta}{\partial t} + \nabla\left(\boldsymbol{V}\cdot\theta - \frac{1}{Pe}\nabla\theta\right) = 0 \tag{3}$$

where:

$\psi$ is such that $u = \dfrac{\partial \psi}{\partial z}$ and $v = -\dfrac{\partial \psi}{\partial x}$;

$\Omega$ is such that $\boldsymbol{\Omega} = \nabla \wedge \boldsymbol{V}$.

To complete these equations, nondimensional initial and boundary conditions from earlier works [30] are used to maintain consistency. This choice allows the effect of the outlet jet angle to be assessed in direct comparison with their results.

Thus, at $t = 0$, the system is in thermal and dynamic equilibrium, with the dimensionless velocity and temperature fields being zero everywhere. This equilibrium is broken by imposing a heat flux on the wall. Then, we have at $t > 0$:

- Fluid flow boundary conditions:

  $u = v = \psi = 0$, $(\boldsymbol{n}\cdot\nabla)\left[(\boldsymbol{n}\cdot\nabla)\psi\right] = -\Omega$, at the solid walls;

  $\Omega = (\boldsymbol{e}_x\cdot\nabla)u = (\boldsymbol{e}_x\cdot\nabla)v = (\boldsymbol{e}_x\cdot\nabla)\psi = 0$ at the inlet;

  $\Omega = 0$, $(\boldsymbol{e}_z\cdot\nabla)\psi = \cos(\sigma)$, $\boldsymbol{V}_{out} = V_{out}\left(\cos(\sigma)\boldsymbol{e}_x + \sin(\sigma)\boldsymbol{e}_z\right)$ at the outlet.

- Thermal conditions:

$$\begin{cases} (\boldsymbol{e}_x\cdot\nabla)\theta = 0 \text{ if } u > 0 \text{ at inlet, and} \\ \theta = 0 \text{ if } u \le 0 \end{cases}$$

$\theta = 0$ along the bottom wall;

$(\boldsymbol{e}_x \cdot \nabla)\theta = 0$ at outlet;

$(\boldsymbol{n} \cdot \nabla)\theta = 0$ along the insulated wall;

$(\boldsymbol{n} \cdot \nabla)\theta = -1$ at the upper horizontal and left vertical walls;

$(\boldsymbol{n} \cdot \nabla)\theta = -\alpha_{gl}$ along the glazing;

$(\boldsymbol{n} \cdot \nabla)\theta = -(\alpha_{PV} \cdot \tau_{gl} - \eta)$ on the PV panel.

where $\bar{n}$ and $\eta$ denote, respectively, the unit normal vector to each wall and the efficiency of the PV cells.

Dimensionless parameters are employed, in particular the Rayleigh number *Ra*, whose variation is used to characterize heat transfer and fluid flow within the domain for each value of the angle $\sigma$. The thermophysical properties of air are assumed to be constant, and the Prandtl number is fixed at 0.71. The Reynolds and Rayleigh numbers are respectively defined as follows:

$$Re = \frac{V_{out} L}{\upsilon} \quad \text{and} \quad Ra = \frac{g\beta\Phi_i L^4}{\lambda\alpha\upsilon}$$

To characterize the heat transfer, the local and average Nusselt numbers are used and defined as follows:

$$Nu = \frac{1}{\theta_P} \quad \text{and} \quad \overline{N_u} = \frac{1}{l}\int_l N_u \mathrm{d}l \tag{4}$$

where $l$ denotes the wall length over which the average value is determined.

The volume flow rate $\dot{V}$ is computed using the formula below:

$$\dot{V} = \int_S \boldsymbol{V} \cdot \boldsymbol{n} \mathrm{d}S \tag{5}$$

where $\boldsymbol{V}$ denotes either the inlet or outlet air velocity, and S is the corresponding inlet or outlet cross-sectional area.

## 2.3. Efficiency of Energy Conversion

The electrical power of the PV is expressed as follows:

$$P_{PV} = \eta\Phi_i S \tag{6}$$

and $\eta$ is calculated using the following expression [31]:

$$\eta = \eta_{ref}\left[1 - \beta_{PV}\left(\overline{T}_{PV} - T_{ref}\right) + \gamma \log \Phi_i\right] \tag{7}$$

Neglecting frictional losses, the electrical power required to drive the fan is assumed to match the kinetic energy $E_k$ of the airflow leaving the chimney. The corresponding expression is:

$$E_k = \frac{1}{2}\dot{m}V_{out}^2 \tag{8}$$

where $\dot{m}$ denotes the mass flow rate of air at the chimney and is determined as follows:

$$\dot{m} = S_c \rho V_{out} \dot{V} \tag{9}$$

where $S_c$ denotes the chimney's cross-sectional area.

### 2.4. Numerical Procedure

To solve the governing equations numerically, the finite volume approach is applied. The computational domain is divided into a number of control volumes $\vartheta$, which serve as the elementary regions for performing the integration. The equations are then written in their integral form for each control volume as follows:

$$\int_{\vartheta}\frac{\partial\phi}{\partial t}\mathrm{d}\vartheta+\int_{\vartheta}\nabla\cdot\left(\boldsymbol{V}\cdot\phi-\xi\cdot\nabla\phi\right)\mathrm{d}\vartheta=\int_{\vartheta}S_{\phi}\mathrm{d}\vartheta \tag{10}$$

where $\phi\in\{\psi,\theta,\Omega\}$, $S_{\phi}$ and $\xi$ represent the physical quantities, the source term and the diffusion coefficient, respectively. The temporal term of the equation is discretized using the implicit Euler scheme, while the spatial terms are handled using the finite volume method. The coefficients of the resulting algebraic equations are calculated using the power-law scheme developed by Patankar [32]. The overall system, completed by boundary conditions discretized via the finite difference method, was implemented in a Fortran-based computational code using the Gauss-Seidel iterative method with under-relaxation.

## 3. Results

### 3.1. Code Validation

A uniform computational grid with dimensions of 101 × 91 and a time increment of $\Delta t=5\times10^{-5}$ is utilized. The convergence condition is defined by a relative difference of $10^{-5}$ between two consecutive iterations. Using these numerical parameters, the developed code is validated under the study conditions defined by Raji and Hasnaoui [33], which are similar to the present rectangular cavity configuration, except for the absence of the chimney. The numerical code is further assessed using the conditions established by Saha *et al.* [34], who investigated mixed convection within a ventilated rectangular enclosure heated from the bottom and thermally insulated on the remaining walls. **Figure 2** and **Figure 3** present the comparisons, highlighting a good agreement between the results obtained and those reported in [33] [34].

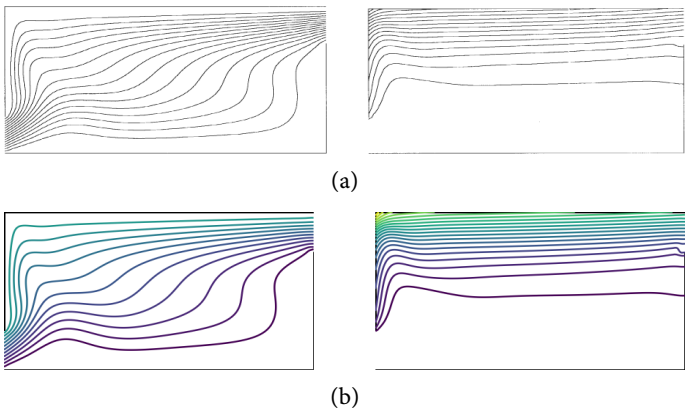

**Figure 2.** Streamline (left) and isotherms (right) plots for $Re = 100$ and $Ra = 10^6$: comparison between the numerical results reported by Raji and Hasnaoui [33] (a) and those obtained using the present computational code (b).

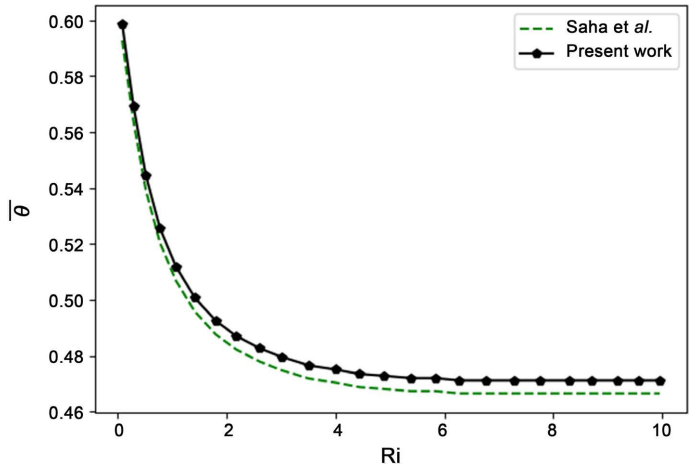


**Figure 3.** Variation of the average dimensionless fluid temperature with Richardson number: Comparison between the numerical results reported by Saha *et al.* [34] and those obtained by the present computational code for $Re = 50$.

## 3.2. Discussions

The computational conditions are defined such that the Reynolds number is fixed at $Re = 50$, while the Rayleigh number varies from $10^3$ to $5 \times 10^5$. This study uses the same configuration as described in earlier work [30], with the chimney inclined at 9˚ to the horizontal and the air jet aligned parallel ($\sigma = 0^\circ$) to the chimney walls. Results from that case show that, for $Re > 45$, complete air renewal within the system is achieved. This setup is therefore used as the reference case for assessing how different jet deviations from the chimney axis affect system performance. The misalignment angles $\sigma$ considered in this study range from 0˚ to 66˚. All other computational parameters are identical to those presented in Table 1 of reference [30].

### 3.2.1. Analysis of Flow and Thermal Fields as a Function of Jet Inclination Angle

**Figures 4-8** present, for each jet velocity inclination angle, the flow fields (streamlines on the left) and temperature fields (isotherms on the right) obtained for three Rayleigh numbers: $Ra = 10^3$, $5 \times 10^4$, and $5 \times 10^5$.

For $\sigma = 0^\circ$ and 21˚, the flow field is characterized by well-organized streamlines forming an almost parallel pattern with respect to one another and to the cavity walls for $Ra = 10^3$ and $5 \times 10^4$ (see **Figure 4(a)**, **Figure 4(b)**, **Figure 5(a)**, and **Figure 5(b)**). In these cases, the regime is clearly dominated by forced convection, with the flow mainly governed by the momentum imposed by the fan. The cold air enters the cavity at a relatively high speed, then changes direction near the opposite wall before being extracted through the chimney outlet. In contrast, at $Ra = 5 \times 10^5$, the streamlines exhibit an upward deflection, indicating the increasing influence of buoyancy forces. The resulting mixed convection regime, combining both forced and natural convection, enhances the effectiveness of air renewal. The associated isotherms display a hump-shaped pattern at the chimney inlet, reflecting the penetration depth of the cold air into the cavity, especially at

lower Rayleigh numbers. Moreover, the vertical stacking of the isotherms and their clustering near the top wall reveal a pronounced thermal stratification, characterized by heat accumulation in the upper region of the cavity.

When the misalignment exceeds 21˚, secondary flow structures begin to develop. For $Ra = 10^3$, a vortex forms at the chimney inlet, growing in size with $\sigma$ and partially obstructing the duct (see **Figure 7(a)** and **Figure 8(a)**). As natural convection becomes stronger, this vortex diminishes slightly but remains embedded at the inlet, particularly at higher misalignment (see **Figure 7(b)** and **Figure 8(b)**). Concurrently, a second unstable vortex appears in the upper right corner of the cavity. Although it disappears rapidly as *Ra* increases, the embedded vortex persists and disrupts the evacuation of warm air, as indicated by the reduced number of open streamlines reaching the outlet. This behavior is most evident for $Ra = 5 \times 10^5$ and angles $\sigma = 51^\circ$ and 66˚, where reverse flow is observed: a portion of the incoming air exits directly through the inlet, severely disrupting air renewal within the cavity (see **Figure 7(c)** and **Figure 8(c)**). The corresponding isotherms reveal a highly stratified temperature distribution in the cavity. Near the lower horizontal wall, where the lowest temperature is imposed, the isotherms rise gradually, indicating overall warming due to insufficient ventilation. In the chimney, the widely spaced isotherms reflect a low temperature gradient and, consequently, a less effective heat transfer process.

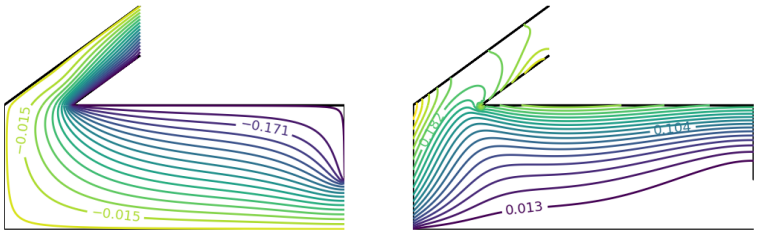


(a) $Ra = 10^3$

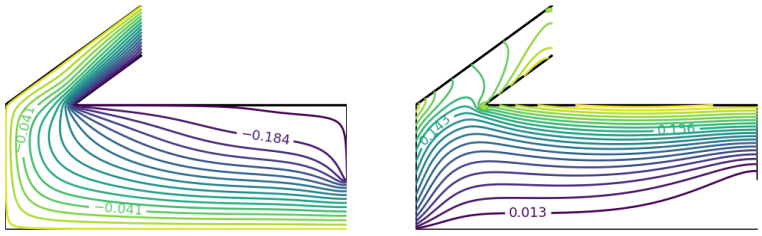


(b) $Ra = 5 \times 10^4$

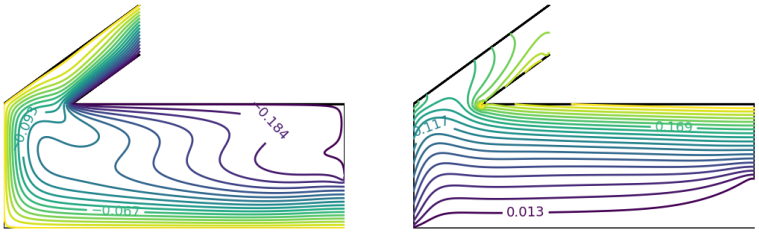


(c) $Ra = 5 \times 10^5$

**Figure 4.** Streamline (left) and isotherms (right) plots for $\sigma = 0^\circ$.

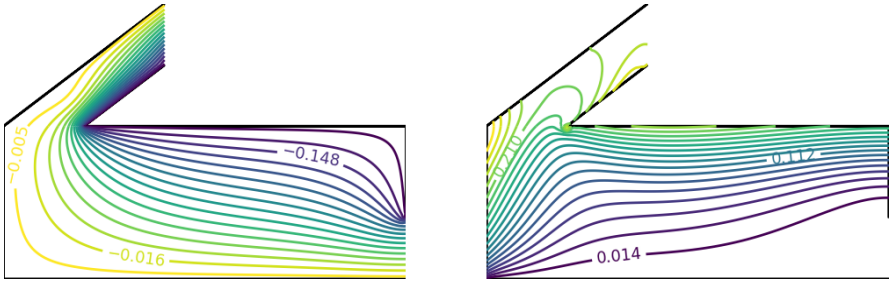


(a) $Ra = 10^3$

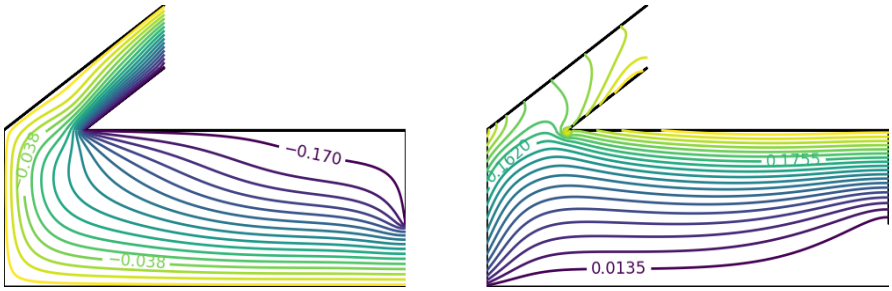


(b) $Ra = 5 \times 10^4$

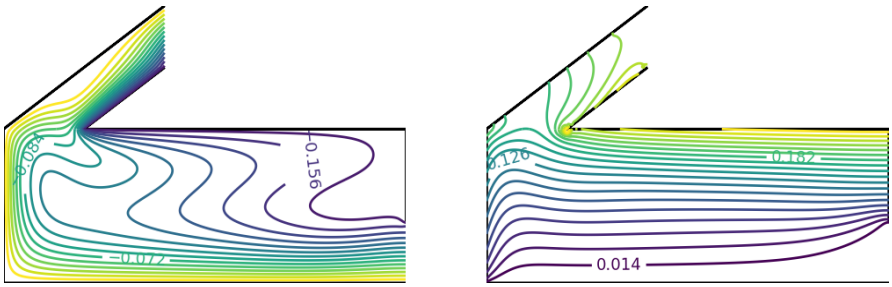


(c) $Ra = 5 \times 10^5$

**Figure 5.** Streamline (left) and isotherms (right) plots for $\sigma = 21^\circ$.

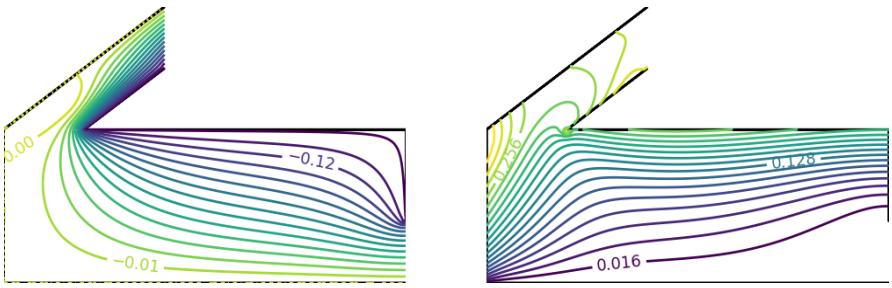


(a) $Ra = 10^3$

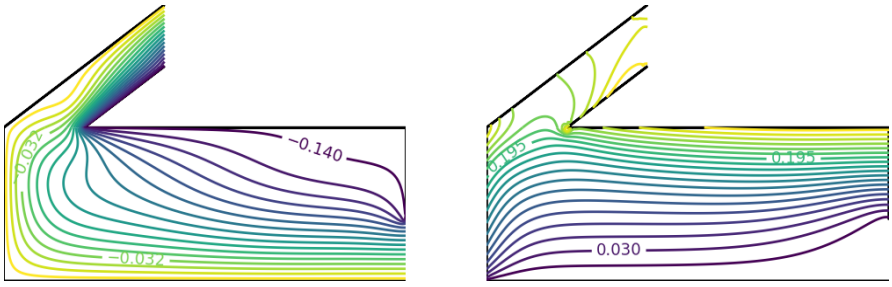


(b) $Ra = 5 \times 10^4$

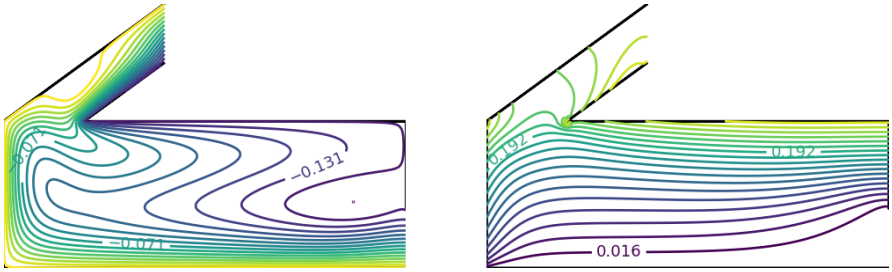


(c) $Ra = 5 \times 10^5$

**Figure 6.** Streamline (left) and isotherms (right) plots for $\sigma = 36^\circ$.

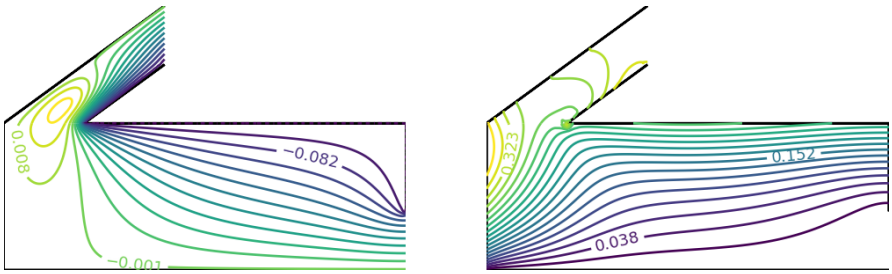


(a) $Ra = 10^3$

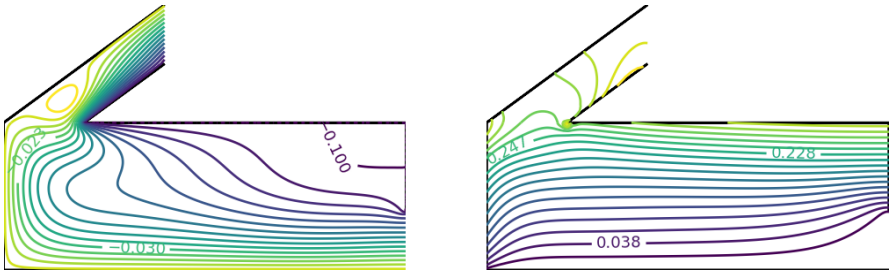


(b) $Ra = 5 \times 10^4$

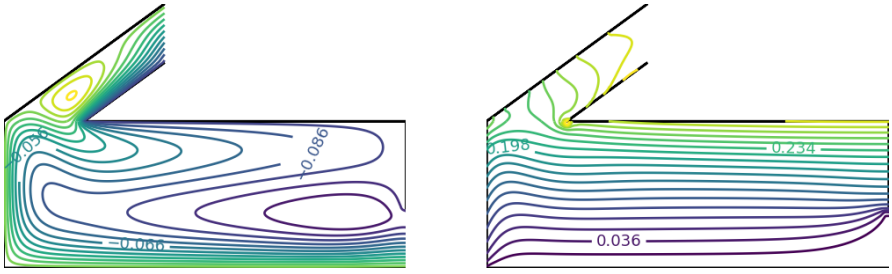


(c) $Ra = 5 \times 10^5$

**Figure 7.** Streamline (left) and isotherms (right) plots for $\sigma = 51^\circ$.

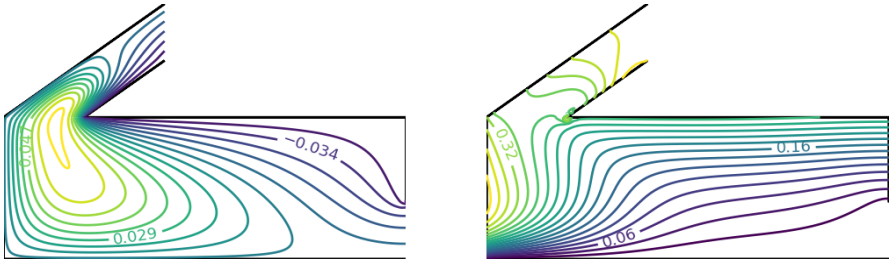


(a) $Ra = 10^3$

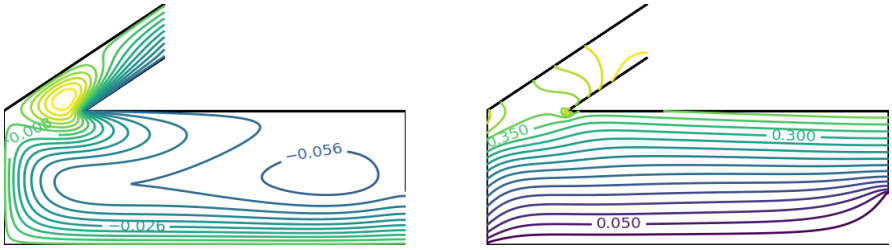


(b) $Ra = 5 \times 10^4$

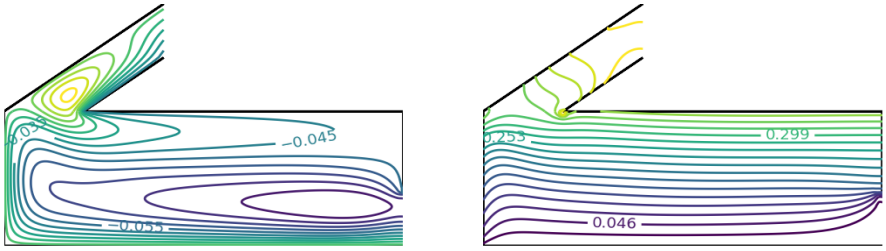


(c) $Ra = 5 \times 10^5$

**Figure 8.** Streamline (left) and isotherms (right) plots for $\sigma = 66^\circ$.

### 3.2.2. Mean Values of Nusselt Number, Dimensionless Temperature, and Volume Flow Rate

To complement the qualitative analysis of flow structures and thermal fields, a quantitative investigation was carried out using the average Nusselt number, the dimensionless mean temperature, and the dimensionless volume flow rate. The heat transfer rate between the channel air and the photovoltaic panel is presented in **Figure 9**. A moderate increase in heat exchange is observed for $Ra < 3 \times 10^4$ and for deviations $\sigma < 36°$. Forced convection dominates the transfers under these conditions, with the flow primarily controlled by the fan-imposed velocity. However, for larger deviations ($\sigma = 51^\circ$ and $66^\circ$), a sharp increase in heat transfer is observed, attributed to thermal instabilities that induce the formation of secondary flows, notably recirculation zones. These zones enhance thermal mixing, leading to a sudden rise in heat transfer. Considering the evolution of the average Nusselt number over the entire range of *Ra* values, it is noted that for $\sigma < 36^\circ$, Nu increases moderately under the influence of buoyancy. In contrast, for $\sigma \geq 36^\circ$, Nu decreases, indicating a reduction in the heat exchange rate between the air and the panel. This decrease is explained by the partial obstruction at the chimney entrance, which limits airflow and consequently heat transfer, resulting in heat accumulation on the panel. Conversely, the evolution of average temperatures, shown in **Figure 10** and **Figure 11**, reveals that for $\sigma < 36^\circ$, the average panel and living space temperatures decrease and then tend to stabilize as *Ra* increases. This behavior illustrates the predominance of forced convection, with relatively high-velocity fresh air efficiently removing heat from both the panel and the living space. For $\sigma \geq 36^\circ$, the temperature initially decreases but then rises for $Ra > 3 \times 10^4$ due to the development of unstable convective cells. A $66^\circ$ misalignment can even cause a 75% increase in the average living space temperature, highlighting the significant impact of jet deviation on thermal performance.

Inlet and outlet flow rates are key indicators for evaluating the ventilation performance of the system under study. Figure 12 shows the outlet flow rates for different deviations $\sigma$. Since the outlet is controlled by a constant imposed velocity, the outlet flow rate, according to Equation (5), is expected to remain constant. It is slightly higher when the jet deviation from the chimney axis is smaller. Figure 13, in contrast, illustrates the variations of the inlet flow rate as a function of the Rayleigh number. For deviations $\sigma \leq 36^{\circ}$, the inlet flow rate increases moderately with *Ra*, consistent with previous studies [11] [13] [35] that reported a rise in volume flow rate with the Rayleigh number. Nevertheless, the inlet flow rate generally remains slightly below the theoretical outlet flow rate, which may be attributed to thermal stratification that slows down the flow. When $\sigma$ exceeds 36˚, the inlet flow rate becomes unstable and exhibits significant fluctuations characterized by abrupt increases. These fluctuations are associated with the inherently unstable flow structure, involving the formation and disappearance of vortices. In some cases, the inlet flow rate even surpasses the controlled outlet flow rate, particularly beyond critical Rayleigh numbers ($1.5 \times 10^5$ for $\sigma = 51^{\circ}$ and $5.1 \times 10^4$ for $\sigma = 66^{\circ}$). This situation clearly indicates the formation of a recirculation loop, in which part of the air exits through the cavity inlet opening.

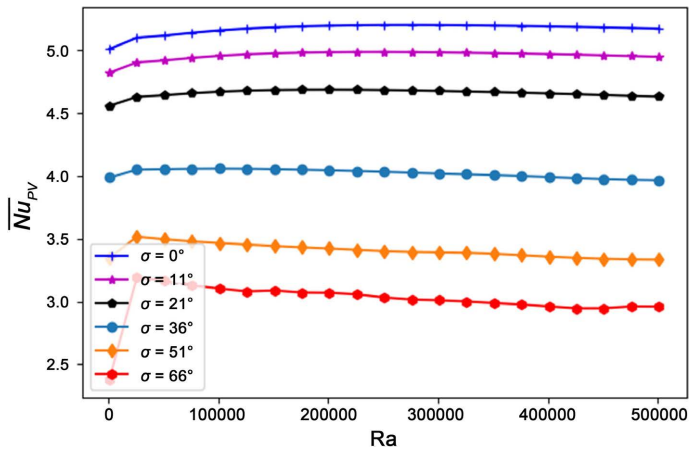


Figure 9. Average Nusselt number calculated on PV.

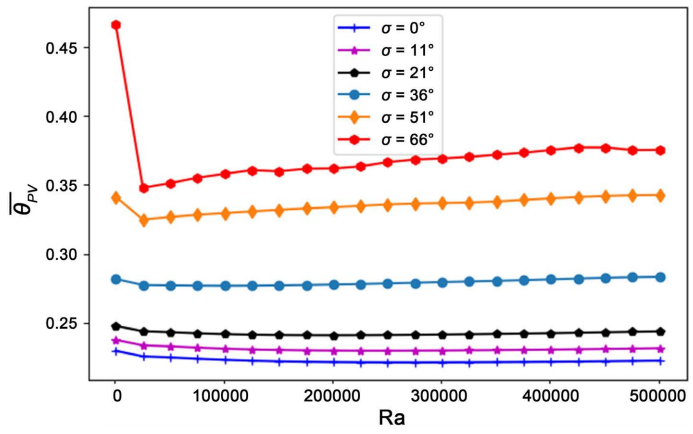


Figure 10. Dimensionless average temperature of the PV.

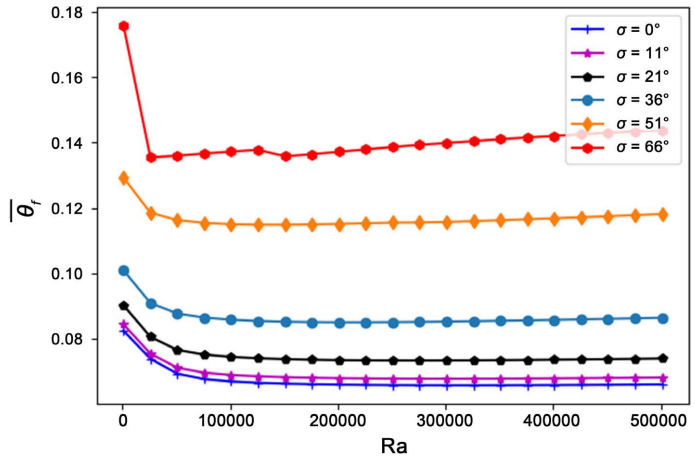


**Figure 11.** Dimensionless average temperature of the living space.

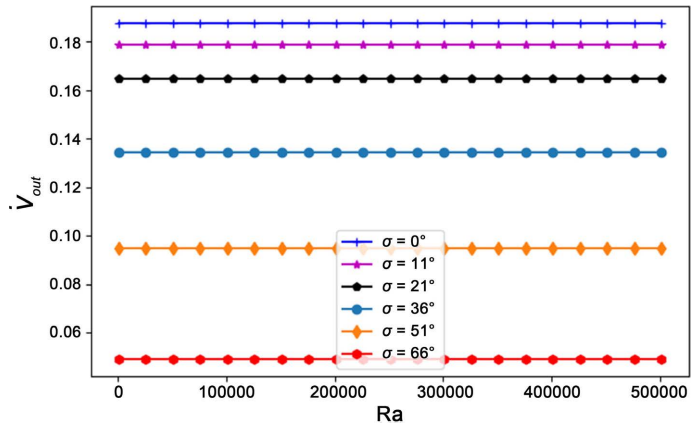


**Figure 12.** Dimensionless outflow rate.

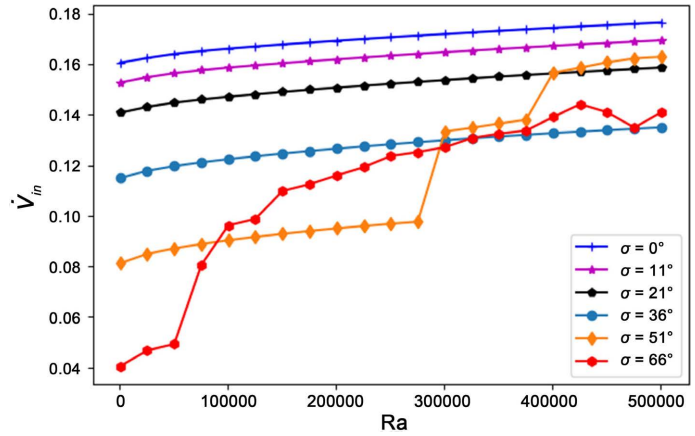


**Figure 13.** Dimensionless inflow rate.

### 3.2.3. Effect of Jet Misalignment on the Ratio of Fan Power to Photovoltaic Power Output

Figure 14 shows the fraction of electrical power consumed by the fan, in comparison with earlier findings [30]. This fraction varies with the jet misalignment relative to the chimney axis. It is important to clearly state that the electrical power

required by the fan is strictly constant in all cases, since the Reynolds number is fixed. Consequently, the observed variation of this fraction is solely due to a decrease in the electrical power generated by the photovoltaic panel. This decrease results from insufficient ventilation of the panel under misaligned jet conditions, leading to panel overheating. As widely documented, an increase in photovoltaic cell temperature causes a reduction in electrical efficiency [36] [37], which directly degrades the overall system performance.

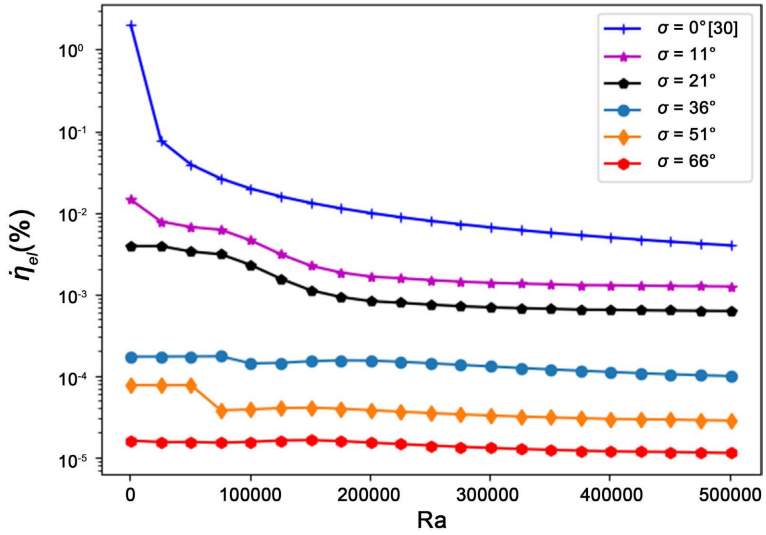


**Figure 14.** The fraction of photovoltaic power consumed by the fan.

## 4. Conclusion

This study models, under the Boussinesq approximation, the heat transfer and airflow within a building incorporating a photovoltaic chimney connected to an extractor fan. The ventilation system operates autonomously by combining buoyancy-driven flow with a kinetic impulse applied at the chimney outlet by the extractor. The angle of this imposed velocity was identified as a key parameter. Numerical solutions of the governing equations were obtained using the finite volume method, implemented in a Fortran-based code. Simulation results show that the efficiency of an active photovoltaic chimney strongly depends on the alignment of the forced air jet with the duct axis. For small deviation angles ( $\sigma \le 21^{\circ}$ ), the flow remains stable, air renewal is effective, and heat transfer is optimal. Beyond 21˚, vortices and reverse flows appear, disrupting ventilation and reducing heat transfer, with a thermal impact reaching up to 75% for $\sigma = 66^{\circ}$. From a practical design perspective, these findings indicate that, irrespective of chimney inclination, the axial fan should be installed in a nearly parallel alignment with the duct, with a maximum allowable misalignment of 21˚, in order to ensure efficient ventilation and optimal thermal performance.

Some limitations of the present study should nevertheless be acknowledged. The adopted modeling assumptions, including two-dimensional laminar flow and the Boussinesq approximation, define the range of validity of the results. In addi-

tion, the use of the vorticity–stream function formulation inherently eliminates the pressure field. However, under real operating conditions, meteorological variations may induce fluctuations in pressure and inlet air velocity, which could influence system performance. Therefore, caution is required when extrapolating the present results to full-scale applications. Furthermore, the assumption of a constant heat flux does not account for temporal variations in solar radiation, which may also affect system performance.

## Conflicts of Interest

The authors declare no conflicts of interest regarding the publication of this paper.

## References

[1] Miyazaki, T., Akisawa, A. and Kashiwagi, T. (2006) The Effects of Solar Chimneys on Thermal Load Mitigation of Office Buildings under the Japanese Climate. *Renewable Energy*, **31**, 987-1010. https://doi.org/10.1016/j.renene.2005.05.003

[2] Zha, X., Zhang, J. and Qin, M. (2017) Experimental and Numerical Studies of Solar Chimney for Ventilation in Low Energy Buildings. *Procedia Engineering*, **205**, 1612-1619. https://doi.org/10.1016/j.proeng.2017.10.294

[3] Abdeen, A., Serageldin, A.A., Ibrahim, M.G.E., El-Zafarany, A., Ookawara, S. and Murata, R. (2019) Solar Chimney Optimization for Enhancing Thermal Comfort in Egypt: An Experimental and Numerical Study. *Solar Energy*, **180**, 524-536. https://doi.org/10.1016/j.solener.2019.01.063

[4] Belfegas, B., Larbi, S. and Tayebi, T. (2021) Experimental and Theoretical Investigation on a Solar Chimney System for Ventilation of a Living Room. *Mathematical Modelling of Engineering Problems*, **8**, 259-266. https://doi.org/10.18280/mmep.080213

[5] Mathur, J., Mathur, S. and Anupma, (2006) Summer-Performance of Inclined Roof Solar Chimney for Natural Ventilation. *Energy and Buildings*, **38**, 1156-1163. https://doi.org/10.1016/j.enbuild.2006.01.006

[6] Ahmed, O.K. and Hussein, A.S. (2018) New Design of Solar Chimney (Case Study). *Case Studies in Thermal Engineering*, **11**, 105-112. https://doi.org/10.1016/j.csite.2017.12.008

[7] Klimeš, L., Charvát, P. and Hejčík, J. (2018) Comparison of the Energy Conversion Efficiency of a Solar Chimney and a Solar PV-Powered Fan for Ventilation Applications. *Energies*, **11**, Article 912. https://doi.org/10.3390/en11040912

[8] Lei, Y., Zhang, Y., Wang, F. and Wang, X. (2016) Enhancement of Natural Ventilation of a Novel Roof Solar Chimney with Perforated Absorber Plate for Building Energy Conservation. *Applied Thermal Engineering*, **107**, 653-661. https://doi.org/10.1016/j.applthermaleng.2016.06.090

[9] Mokheimer, E.M.A., Shakeel, M.R. and Al-Sadah, J. (2017) A Novel Design of Solar Chimney for Cooling Load Reduction and Other Applications in Buildings. *Energy and Buildings*, **153**, 219-230. https://doi.org/10.1016/j.enbuild.2017.08.011

[10] He, G. and Lv, D. (2022) Distributed Heat Absorption in a Solar Chimney to Enhance Ventilation. *Solar Energy*, **238**, 315-326. https://doi.org/10.1016/j.solener.2022.04.047

[11] Ren, X., Liu, R., Wang, Y., Wang, L. and Zhao, F. (2019) Thermal Driven Natural Convective Flows Inside the Solar Chimney Flush-Mounted with Discrete Heating

Sources: Reversal and Cooperative Flow Dynamics. *Renewable Energy*, **138**, 354-367. https://doi.org/10.1016/j.renene.2019.01.090

[12] Imran, A.A., Jalil, J.M. and Ahmed, S.T. (2015) Induced Flow for Ventilation and Cooling by a Solar Chimney. *Renewable Energy*, **78**, 236-244. https://doi.org/10.1016/j.renene.2015.01.019

[13] Ren, X., Wang, L., Liu, R., Wang, L. and Zhao, F. (2021) Thermal Stack Airflows Inside the Solar Chimney with Discrete Heat Sources: Reversal Flow Regime Defined by Chimney Inclination and Thermal Rayleigh Number. *Renewable Energy*, **163**, 342-356. https://doi.org/10.1016/j.renene.2020.08.128

[14] Jing, H., Chen, Z. and Li, A. (2015) Experimental Study of the Prediction of the Ventilation Flow Rate through Solar Chimney with Large Gap-to-Height Ratios. *Building and Environment*, **89**, 150-159. https://doi.org/10.1016/j.buildenv.2015.02.018

[15] Mehdipour, R., Golzardi, S. and Baniamerian, Z. (2020) Experimental Justification of Poor Thermal and Flow Performance of Solar Chimney by an Innovative Indoor Experimental Setup. *Renewable Energy*, **157**, 1089-1101. https://doi.org/10.1016/j.renene.2020.04.158

[16] N'Tsoukpoe, K.E. (2022) Effect of Orientation and Tilt Angles of Solar Collectors on Their Performance: Analysis of the Relevance of General Recommendations in the West and Central African Context. *Scientific African*, **15**, e01069. https://doi.org/10.1016/j.sciaf.2021.e01069

[17] Uba, F.A. and Sarsah, E.A. (2013) Optimization of Tilt Angle for Solar Collectors in WA, Ghana. *Advances in Applied Science Research*, **4**, 108-114.

[18] Ekoe A Akata, A.M., Njomo, D., Agrawal, B., Mackpayen, A. and Ali, A.M. (2022) Tilt Angle and Orientation Assessment of Photovoltaic Thermal (PVT) System for Sub-Saharan Tropical Regions: Case Study Douala, Cameroon. *Sustainability*, **14**, Article 15591. https://doi.org/10.3390/su142315591

[19] Abdallah, A.S.H., Hiroshi, Y., Goto, T., Enteria, N., Radwan, M.M. and Eid, M.A. (2014) Parametric Investigation of Solar Chimney with New Cooling Tower Integrated in a Single Room for New Assiut City, Egypt Climate. *International Journal of Energy and Environmental Engineering*, **5**, Article No. 92. https://doi.org/10.1007/s40095-014-0092-6

[20] Bassiouny, R. and Korah, N.S.A. (2009) Effect of Solar Chimney Inclination Angle on Space Flow Pattern and Ventilation Rate. *Energy and Buildings*, **41**, 190-196. https://doi.org/10.1016/j.enbuild.2008.08.009

[21] Harris, D.J. and Helwig, N. (2007) Solar Chimney and Building Ventilation. *Applied Energy*, **84**, 135-146. https://doi.org/10.1016/j.apenergy.2006.07.001

[22] Kong, J., Niu, J. and Lei, C. (2020) A CFD Based Approach for Determining the Optimum Inclination Angle of a Roof-Top Solar Chimney for Building Ventilation. *Solar Energy*, **198**, 555-569. https://doi.org/10.1016/j.solener.2020.01.017

[23] Ardila, O., Quiroga, J. and Amaris, C. (2023) Assessment of Solar Chimney Potential for Passive Ventilation and Thermal Comfort in the Northeast of Colombia. *Results in Engineering*, **20**, Article ID: 101641. https://doi.org/10.1016/j.rineng.2023.101641

[24] Hou, Y., Li, H. and Li, A. (2019) Experimental and Theoretical Study of Solar Chimneys in Buildings with Uniform Wall Heat Flux. *Solar Energy*, **193**, 244-252. https://doi.org/10.1016/j.solener.2019.09.061

[25] Nguyen, Y.Q. and Wells, J.C. (2020) A Numerical Study on Induced Flowrate and Thermal Efficiency of a Solar Chimney with Horizontal Absorber Surface for Ventilation of Buildings. *Journal of Building Engineering*, **28**, Article ID: 101050. https://doi.org/10.1016/j.jobe.2019.101050

[26] Jaber Khalaf, Z. and M. Jalil, J. (2011) Induced Buoyancy in Inclined Solar Chimney for Natural Ventilation. *Engineering and Technology Journal*, **29**, 183-194. https://doi.org/10.30684/etj.29.2.1

[27] Zamora, B. (2023) A Review on Solar Chimneys: From Natural Convection Fundamentals to Thermohydraulic Best-Performance Proposals. *Processes*, **11**, Article 386. https://doi.org/10.3390/pr11020386

[28] Nguyen, Y.Q. (2018) Studying Convective Flow in a Vertical Solar Chimney at Low Rayleigh Number by Lattice Boltzmann Method: A Simple Method to Suppress the Reverse Flow at Outlet. In: Nguyen-Xuan, H., Phung-Van, P. and Rabczuk, T., Eds., *Proceedings of the International Conference on Advances in Computational Mechanics* 2017, Springer, 807-820. https://doi.org/10.1007/978-981-10-7149-2_57

[29] Khanal, R. and Lei, C. (2012) Flow Reversal Effects on Buoyancy Induced Air Flow in a Solar Chimney. *Solar Energy*, **86**, 2783-2794. https://doi.org/10.1016/j.solener.2012.06.015

[30] Kpode, K., Nougblega, Y., Kata, N. and Samah, H. (2025) Numerical Study of Airflow Optimization and Thermal Performance of Building Equipped with Photovoltaic Chimney. *International Journal of Heat and Technology*, **43**, 1267-1275. https://doi.org/10.18280/ijht.430406

[31] Notton, G., Cristofari, C., Mattei, M. and Poggi, P. (2005) Modelling of a Double-Glass Photovoltaic Module Using Finite Differences. *Applied Thermal Engineering*, **25**, 2854-2877. https://doi.org/10.1016/j.applthermaleng.2005.02.008

[32] Patankar, S. (2018) Numerical Heat Transfer and Fluid Flow. CRC Press. https://doi.org/10.1201/9781482234213

[33] Raji, A. and Hasnaoui, M. (2000) Mixed Convection Heat Transfer in Ventilated Cavities with Opposing and Assisting Flows. *Engineering Computations*, **17**, 556-572. https://doi.org/10.1108/02644400010339770

[34] Saha, S., Saha, G., Ali, M. and Islam, M.Q. (2006) Combined Free and Forced Convection Inside a Two-Dimensional Multiple Ventilated Rectangular Enclosure. *ARPN Journal of Engineering and Applied Sciences*, **1**, 23-35.

[35] Wei, T., Li, H., Sun, R., Yu, C.W. and Luo, X. (2023) Evaluation of Photovoltaic-Based Solar Chimney-Assisted Stack Ventilation within a Large Space Hall: A Case Study. *Indoor and Built Environment*, **33**, 741-756. https://doi.org/10.1177/1420326x231220527

[36] Shaker, L.M., Al-Amiery, A.A., Hanoon, M.M., Al-Azzawi, W.K. and Kadhum, A.A.H. (2024) Examining the Influence of Thermal Effects on Solar Cells: A Comprehensive Review. *Sustainable Energy Research*, **11**, Article No. 6. https://doi.org/10.1186/s40807-024-00100-8

[37] Hudișteanu, V., Chereches, N., Țurcanu, F., Hudișteanu, I. and Romila, C. (2024) Impact of Temperature on the Efficiency of Monocrystalline and Polycrystalline Photovoltaic Panels: A Comprehensive Experimental Analysis for Sustainable Energy Solutions. *Sustainability*, **16**, Article 10566. https://doi.org/10.3390/su162310566

## Nomenclature

| | |
|---|---|
| $\boldsymbol{e}_x, \boldsymbol{e}_z$ | Horizontal and vertical axis |
| $\boldsymbol{V}$ | Dimensionless velocity vector |
| $L$ | Length of the cavity, m |
| $Nu$ | Local Nusselt number along the PV |
| $Pe$ | Péclet number |
| $Pr$ | Prandtl number, $=\nu/\alpha$ |
| $T$ | Dimensionless time |
| $T$ | Temperature, K |
| $u$, $v$ | Horizontal and vertical velocity dimensionless velocity coordinate |
| $x$, $z$ | Horizontal and vertical dimensionless coordinates |

## Greek Symbols

| | |
|---|---|
| $\alpha$ | Thermal diffusivity ($m^2 \cdot s^{-1}$) |
| $\beta$ | Thermal expansion coefficient ($K^{-1}$) |
| $\lambda$ | Thermal conductivity ($W \cdot m^{-1} \cdot K^{-1}$) |
| $\Omega$ | Dimensionless vorticity |
| $\psi$ | Dimensionless stream function |
| $\Phi_i$ | Intensity of solar radiation ($W \cdot m^{-2}$) |
| $\theta$ | Dimensionless temperature |
| $\nu$ | Kinematic viscosity ($m^2 \cdot s^{-1}$) |

## Subscripts

| | |
|---|---|
| f | Fluid |
| p | Wall |
| out | Outlet |
| in | Inlet |